



Efficient Energy Conversion through Vortex Arrays in the Turbulent Magnetosheath

Chuanpeng Hou¹ , Jiansen He¹ , Die Duan¹ , Xingyu Zhu¹ , Wenya Li², Daniel Verscharen³ , Terry Liu⁴ , and Tiejian Wang⁵

¹ School of Earth and Space Sciences, Peking University, Beijing, 100871, People's Republic of China; jshept@pku.edu.cn

² State Key Laboratory of Space Weather, National Space Science Center, Chinese Academy of Sciences, Beijing 100190, People's Republic of China

³ Mullard Space Science Laboratory, University College London, Dorking RH5 6NT, UK

⁴ Department of Earth, Planetary, and Space Sciences, University of California, Los Angeles, Los Angeles, CA 90095, USA

⁵ School of Earth Science, Yunnan University, Yunnan 650091, People's Republic of China

Received 2022 September 14; revised 2023 January 28; accepted 2023 January 31; published 2023 March 22

Abstract

Turbulence is often enhanced when transmitted through a collisionless plasma shock. We investigate how the enhanced turbulent energy in the Earth's magnetosheath effectively dissipates via vortex arrays. This research topic is of great importance as it relates to particle energization at astrophysical shocks across the universe. Wave modes and intermittent coherent structures are the key candidate mechanisms for energy conversion in turbulent plasmas. Here, by comparing in-situ measurements in the Earth's magnetosheath with a theoretical model, we find the existence of vortex arrays at the transition between the downstream regions of the Earth's bow shock. Vortex arrays consist of quasi-orthogonal kinetic waves and exhibit both high volumetric filling factors and strong local energy conversion, thereby showing a greater dissipative energization than traditional waves and coherent structures. Therefore, we propose that vortex arrays are a promising mechanism for efficient energy conversion in the sheath regions downstream of astrophysical shocks.

Unified Astronomy Thesaurus concepts: [Space plasmas \(1544\)](#); [Interplanetary turbulence \(830\)](#); [Planetary bow shocks \(1246\)](#)

Supporting material: interactive figures

1. Introduction

The magnetosheath is an ideal environment to investigate the turbulent dissipation (He et al. 2015b; Wan et al. 2015; Wu et al. 2020) of collisionless plasmas. The hot and dense magnetosheath plasma exhibits greater turbulence amplitudes than the solar wind upstream of the bow shock. These conditions make it easier to accurately measure the fluctuations of the plasma particles and fields (Schwartz et al. 1996). The magnetosheath has thus become an essential territory for several space exploration missions such as Cluster (Escoubert et al. 2001), MMS (Burch et al. 2016a), and other cross-scale constellation programs (Dai et al. 2020) to explore and reveal the physical processes associated with turbulence (He et al. 2015b; Wang et al. 2016; Chen et al. 2019; Wang et al. 2019; Hou et al. 2021) in space plasma. Furthermore, the magnetosheath hosts many wave modes (Schwartz et al. 1996; He et al. 2011; Wu et al. 2016; He et al. 2020) and coherent structures (Tu & Marsch 1995; Drake et al. 2003; Wang et al. 2013; Osman et al. 2014; Wan et al. 2015; Fu et al. 2016; Chasapis et al. 2018), making it a valuable site for studying wave-particle coupling (Chen et al. 2019; Luo et al. 2020) and the dissipation of structures (Burch et al. 2016b; Wang et al. 2019). At kinetic scales, the magnetosheath turbulence shares properties with various wave modes, including ion cyclotron waves (Zhao et al. 2019; Luo et al. 2020), kinetic Alfvén waves (Chen et al. 2019; He et al. 2020), whistler waves (Masood et al. 2006; Huang et al. 2018), mirror modes (Lucek et al. 1999; Soucek et al. 2008; Yao et al. 2018), and kinetic slow

modes (Schwartz et al. 1996; Roberts et al. 2018). Kinetic Alfvén waves are attributed to nonlinear particle trapping (Gershman et al. 2017), turbulent heating (Roberts et al. 2018), and energy input in the Earth's auroral region (Artemyev et al. 2015). In addition, kinetic slow modes are compressible fluctuations that represent pressure-balanced structures (Narita & Marsch 2015) and are attributed to the mode conversion of ultra-low-frequency waves in the downstream of the bow shock (Hao et al. 2018).

Previous research has focused on the physics of a particular wave mode, such as the dissipation of ion cyclotron waves (He et al. 2019; Luo et al. 2020), the compressibility and dissipation of kinetic Alfvén waves (Chen & Boldyrev 2017; Chen et al. 2019; He et al. 2020), the lion's roar of whistler waves (Huang et al. 2018), and the instability of mirror modes (Gary et al. 1993; Lucek et al. 1999; Soucek et al. 2008; Hoilijoki et al. 2016). However, these separate studies of specific wave modes do not provide a comprehensive picture of the magnetosheath turbulence and fail to solve the apparent paradox between the high dissipation rate observed in magnetosheath turbulence and the low dissipation rate predicted by linear plasma theory (He et al. 2020).

Coherent structures, such as current sheets (Sundkvist et al. 2007; Burch et al. 2016b) and magnetic flux ropes (Hasegawa et al. 2012; Wang et al. 2016; Yao et al. 2020), appear more frequently in the magnetosheath than in other space environments. In a similar way as a vortex is the fundamental building block of coherent structures in hydrodynamic turbulence, magnetized vortex structures are the components making up intermittent structures in magnetohydrodynamic (MHD) turbulence. For example, the Alfvén vortex, a typical type of MHD vortex, is found in the solar wind (Lion et al. 2016; Roberts et al. 2016), as well as in terrestrial and planetary space



Original content from this work may be used under the terms of the [Creative Commons Attribution 4.0 licence](#). Any further distribution of this work must maintain attribution to the author(s) and the title of the work, journal citation and DOI.

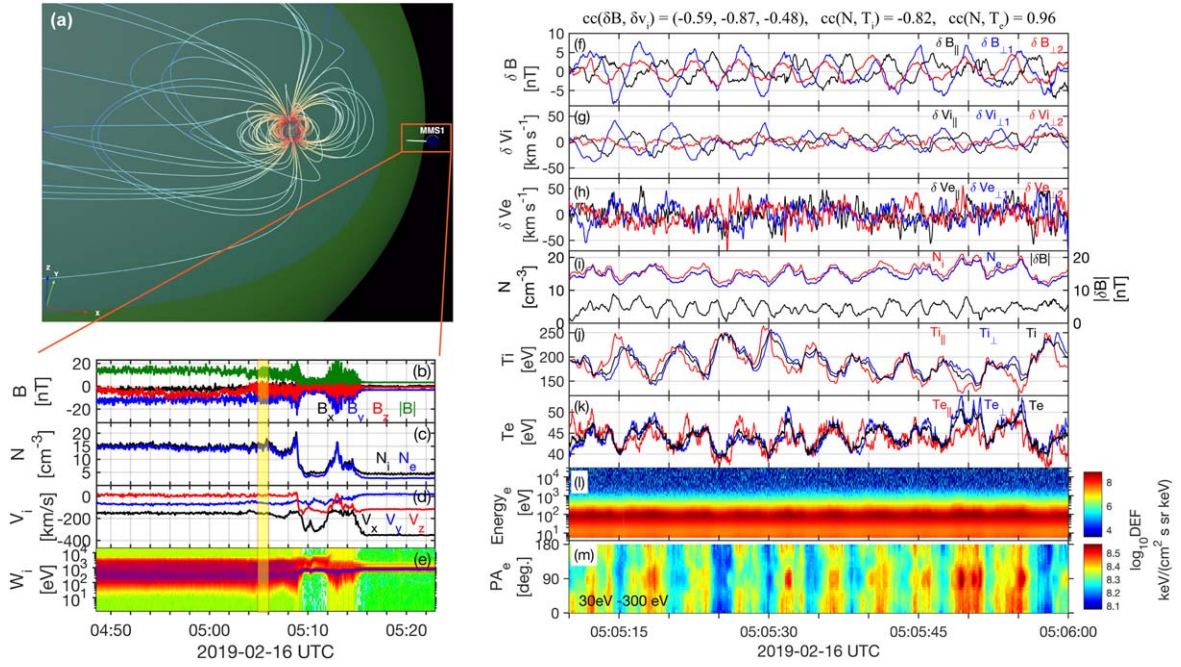


Figure 1. Overview of MMS1 measurements in the Earth’s magnetosheath. (a) Sketch of MMS1 crossing the bow shock from the magnetosheath into the solar wind. (b)–(e) Time series plots of magnetic field components, number density, ion bulk velocity, and differential ion energy flux density over a longer time interval. The yellow area includes the vortex array event. (f) Magnetic field fluctuations. The subscript “||” represents the direction parallel to the background magnetic field. The subscripts “⊥1” and “⊥2” represent the directions perpendicular to the background magnetic field. (g) Ion bulk velocity fluctuations. (h) Electron bulk velocity. (i) Left axis: number density of ions and electrons; Right axis: magnitude of magnetic field vector fluctuations. (j) Ion temperature. (k) Electron temperature. (l) Differential electron energy flux density. (m) Pitch angle distribution of electrons.

environments (Sundkvist et al. 2005; Alexandrova et al. 2006). There is a long-standing important question about the coexistence of coherent structures and wave-like fluctuations in magnetosheath turbulence: are wave-like fluctuations and intermittent coherent structures independent of each other or interconnected?

Here, we report observations of a vortex array and reveal that it is composed of orthogonal wave modes with their wavevectors mainly perpendicular to the background magnetic field. We point out that the vortex array is more efficient than unidirectionally propagating wave-like turbulence in dissipating the turbulence energy. We present the corresponding particle kinetics associated with the energy conversion of the vortex array. Combining both the high volumetric filling factor of wave-like fluctuations and the high energy conversion rate of coherent structures, vortex arrays play a potentially essential role in the energy conversion and energization of space plasma turbulence. This paper is organized as follows: In Section 2, we introduce the observed vortex array event. We show the comparison between our observations and our model in Section 3. Section 4 presents our summary and a discussion.

2. Vortex Array Event

During 05:00 and 05:20 UTC on 2019 February 16, the Magnetospheric Multiscale (MMS) satellites traveled from the magnetosheath into the solar wind after crossing the Earth’s bow shock (Figure 1(a)) and measured the related variations in the magnetic field and plasma (Figures 1(b)–(e)). The interplanetary magnetic field lines are oriented almost along the y -direction in geocentric solar ecliptic coordinates (see Figure 1(b)). Therefore, we identify the bow shock as quasi-perpendicular near the nose and quasi-parallel on both flanks in this event. According to the position of MMS (Figure 1(a)) and

by comparing the magnetic field perturbations near the various shock geometries (Figure 2), we find that MMS crossed the transition zone between quasi-parallel and quasi-perpendicular geometry on the downstream side of the shock in this event.

In the magnetosheath downstream of the bow shock (see Figures 1(b)–(e) highlighted in yellow), MMS observed quasi-periodic wave-like fluctuations with a period of about 5 s as seen in a synopsis of the measured quantities (Figures 1(f)–(m)), including the magnetic field, number density, bulk velocity, temperature, differential electron energy flux density, and the electron pitch angle distribution in a Field-aligned Coordinate system. In this coordinate system, the parallel direction is defined as a unit vector, \mathbf{e}_B , and the other two perpendicular directions ($\perp 1$ and $\perp 2$) are defined as the unit vectors $\mathbf{e}_{\nu \times B}$ and $\mathbf{e}_{B \times (\nu \times B)}$, respectively, where the subscript B represents the background magnetic field vector calculated as the time-averaged magnetic field vector and ν represents the time-averaged ion fluid velocity vector.

The magnetic field (Figure 1(f)) and ion bulk velocity (Figure 1(g)) exhibit a component-wise anticorrelation with correlation coefficients for the three components being $(-0.59, -0.87, -0.48)$ consistent with the sense of Alfvénic fluctuations around kinetic scales. Since the correlation coefficients are notably less than 1, other wave modes are likely to contribute to the fluctuations besides the kinetic Alfvén waves (KAWs). The number density of ions and electrons exhibits a strong perturbation ($\frac{\delta n}{n_0} \sim 0.25$) (see Figure 1(i)); so the fluctuations also have a contribution from highly compressive modes, such as kinetic slow-mode waves (KSWs), which exist in the downstream region of the quasi-parallel shock (Hao et al. 2018). Our calculations show that the temperature anisotropy of ions crosses the threshold of the mirror-mode instability, the evolution of which at kinetic scales in the nonlinear stage can

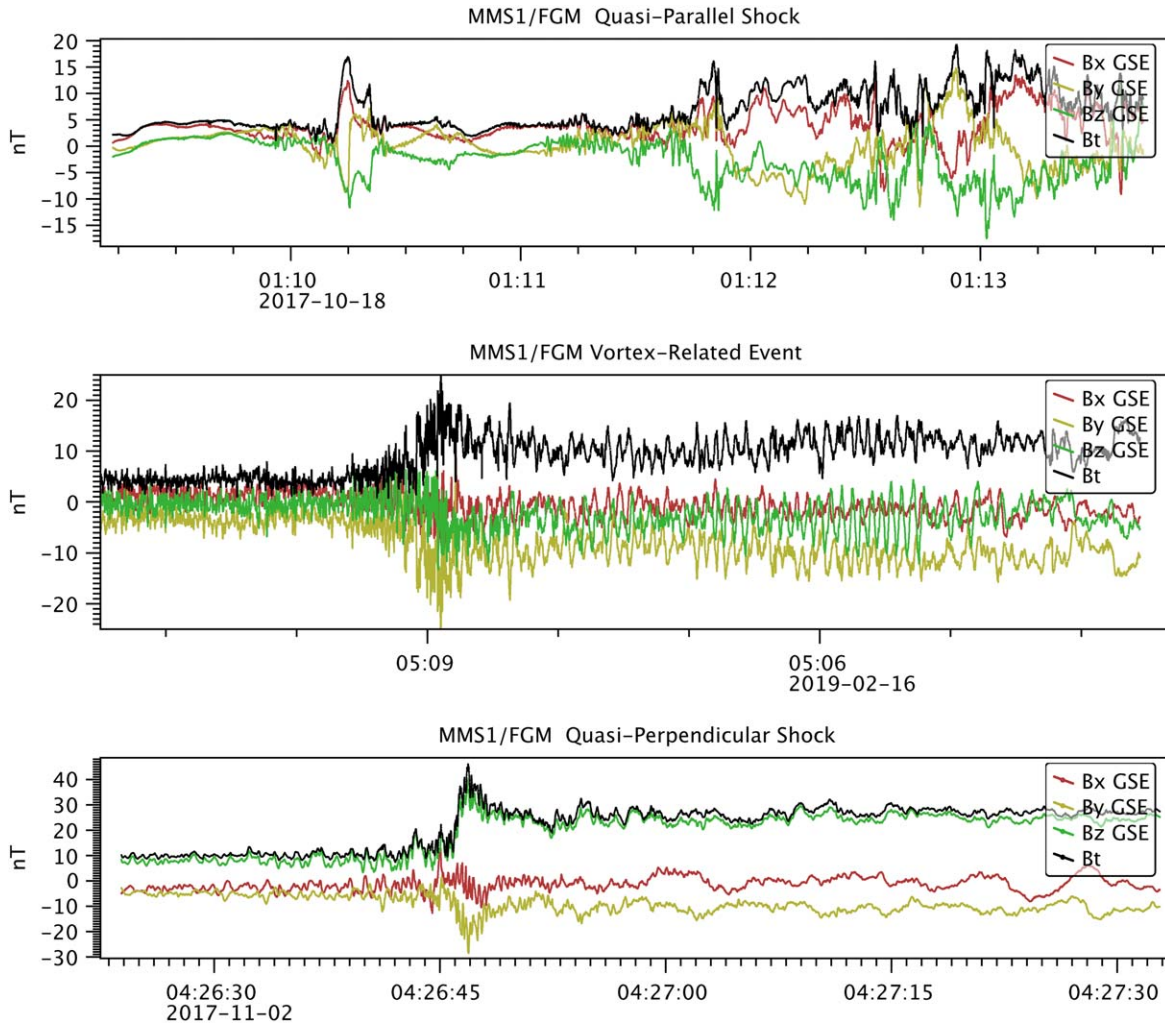


Figure 2. Comparison of magnetic field perturbations for typical quasi-parallel and quasi-perpendicular shock geometries with a vortex. (Top) The quasi-parallel shock shows strong magnetic field perturbations but no pronounced shock ramp. (Bottom) The quasi-perpendicular shock shows only weak magnetic field perturbations but a significant shock ramp. (Middle) The magnetic field perturbations in our vortex-related shock and its jump characteristics lie between the quasi-parallel and quasi-perpendicular extremes, indicating that MMS crossed the transition zone between the two extreme shock geometries.

generate a pair of KAWs (Wu et al. 2001), and which is usually characteristic of the downstream region of quasi-perpendicular shocks. Oblique KAWs and KSWs show an anticorrelation between density and magnetic field strength, while they differ remarkably from each other in other aspects, e.g., magnetic compressibility and Alfvén ratio (Zhao et al. 2014b). According to linear theory, the magnetic compressibility of KAWs is significantly less than that of KSWs, and the magnetic compressibility of KAWs (KSWs) increases (decreases) with increasing wavenumber (Zhao et al. 2014b). The Alfvén ratio ($R_A = \langle |\delta v|^2 \rangle / \langle |\delta v_B|^2 \rangle$, where δv is the fluctuation of the plasma bulk velocity, and δv_B is the fluctuation of the magnetic field in units of the Alfvén speed, of KAWs is less than that of KSWs, while R_A of KAWs (KSWs) decreases (increases) with increasing wavenumber (Zhao et al. 2014b). Based on these properties, Hao et al. 2018 successfully distinguish KSWs downstream of the quasi-parallel shock in simulations. In our observed event, the magnetic compressibility is greater at large scales, and R_A increases and then decreases with decreasing scales. Based on the characteristics of magnetic compressibility and the Alfvén ratio in our observations, in Section 3, we set up a synthetic wave model with KSWs at larger and KAWs at smaller scales. In addition, the ion and electron number

densities are almost equal, satisfying the plasma quasi-neutrality condition. We also recognize that the fluctuations in the magnetic field disturbance magnitude $|\delta \mathbf{B}|$ (Figure 1(f)) have twice the frequency of the other fluctuating variables (e.g., magnetic field components, velocity components, and number densities). In the following section, we see that a simple model based on KAWs and KSWs is consistent with these observed features.

There is a strong correlation between the number density and the particle temperatures, with a correlation coefficient of -0.82 for ions and 0.96 for electrons. The ion temperature (Figure 1(j)) is positively correlated with the ion number density (Figure 1(i)), while the electron temperature (Figure 1(k)) is anticorrelated with the electron number density (Figure 1(i)), suggesting that the ions and electrons undergo opposite phases of their heating and cooling processes. Similarly, the electron energy spectral flux density (Figure 1(g)) is modulated with quasi-periodic patterns, especially around an energy of 100 eV. The distribution of electron pitch angles (Figure 1(h)) is periodically concentrated around 90° , which is characteristic of trapped particles, as it is known for magnetic mirror structures, for instance. The electron thermal anisotropy (Figure 1(k)) also shows this

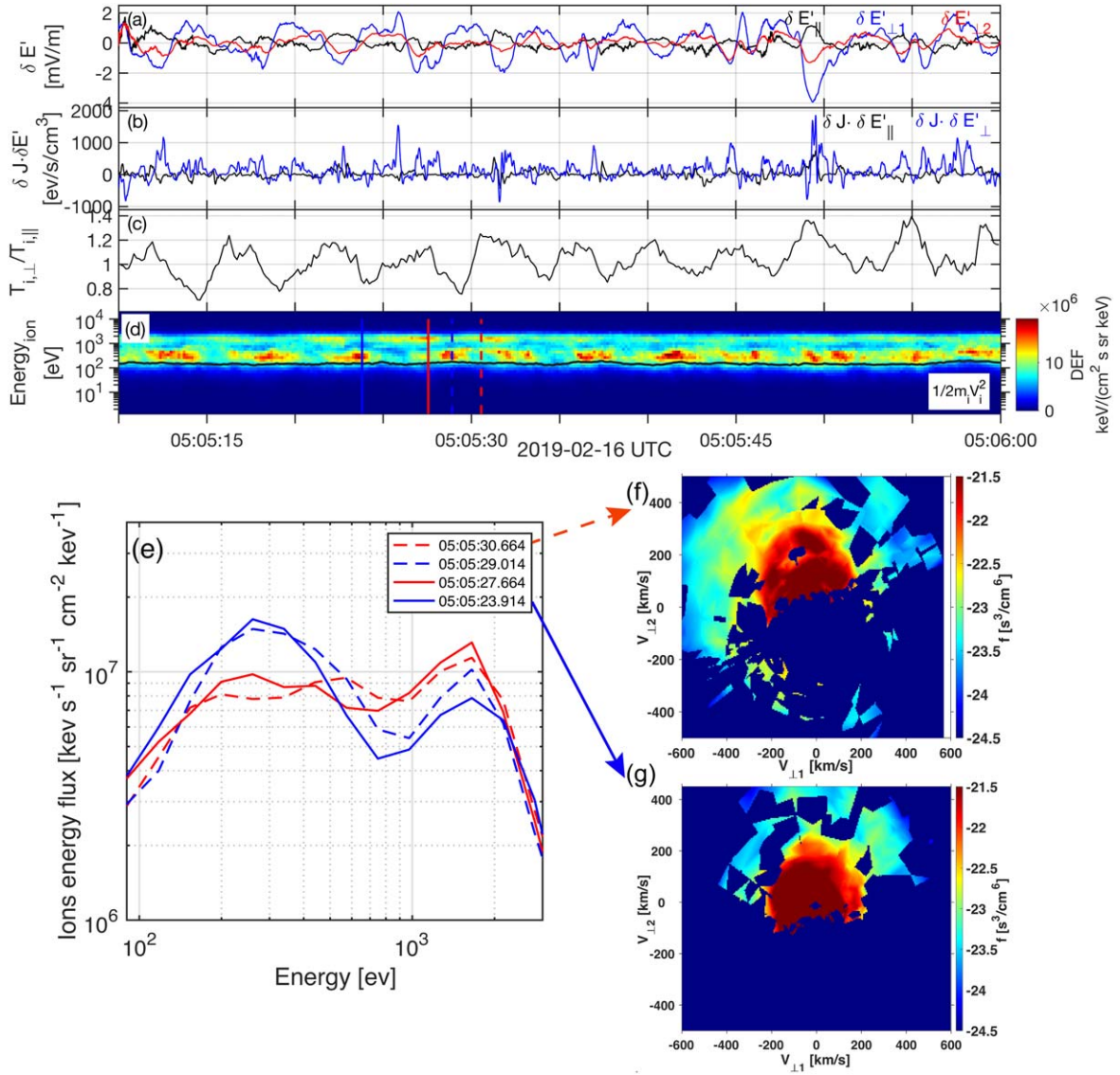


Figure 3. MMS1 observations of energy conversion and ion energy spectrum. (a) Electric field fluctuation ($\delta E' = \delta(\mathbf{E}_{sc} + \mathbf{V}_i) \times \mathbf{B}$). (b) Energy conversion by the total current. (c) Anisotropy of the ion temperature. (d) Differential ion energy flux density. The black line represents the ion bulk energy. The different curves represent four time instances corresponding to the labels in (e). (e) The energy spectrum of ions for the four time instances highlighted in (d). For the red and blue curves, the energy flux shows different peak positions. (f) and (g) Velocity distributions of ions in the field-perpendicular plane for two time instances. Compared to (g), (f) shows a wider distribution and higher perpendicular ion temperature. The corresponding animations of panels (d), (f), and (g) are available in the online version of this paper. This animation shows the velocity distribution of ions in the perpendicular plane at different times. The animation runs from 05:05:10–05:06:00 at a separation of 1.5 s between adjacent steps.

trapped-particle pattern. An important aspect is that this event exhibits stronger energy conversion (positive $\delta \mathbf{J} \cdot \delta \mathbf{E}'$) in the perpendicular direction (Figure 3(b)), with the fluctuating current density $\delta \mathbf{J}$ being calculated from the charge-density weighted fluid velocity difference of the plasma species. Considering the observed Alfvénicity and compressibility, we speculate that a combination of KAWs and KSWs contributes to the observed fluctuations and introduces a strong energy conversion in the perpendicular direction. This behavior is different from the traditional Landau damping of KAWs that thermalizes mostly in the parallel direction.

The periodic fluctuations in the ion temperature anisotropy (Figure 3(c)) and the ion energy spectrum (Figure 3(d)) are also associated with the oscillating wave-like fluctuations. We compare the ion temperature anisotropy and the ion energy spectrum at four time instances corresponding to the peaks (red

lines in Figure 3(d)) and valleys (blue lines in Figure 3(d)) of the temperature anisotropy. The differential energy flux density related to the four instances is shown in Figure 3(e). At the peak of the ion temperature anisotropy, we see an increase of ion energy flux density at higher energy (Figure 3(e)), and the ion distribution has a more extensive spread in velocity space (Figure 3(f)), which corresponds to a higher perpendicular temperature. At the time of the temperature anisotropy valley, the ion energy flux density is concentrated at lower energies (Figure 3(e)), and the spread of the distribution is smaller (Figure 3(g)). The above characteristics suggest that the enhancement of ion temperature anisotropy and ion energization are in phase.

Moreover, we compare the periodic oscillations and phases of the electric field in the plasma reference frame ($\delta E'$) (Figure 3(a)), the energy transfer rate between fields and

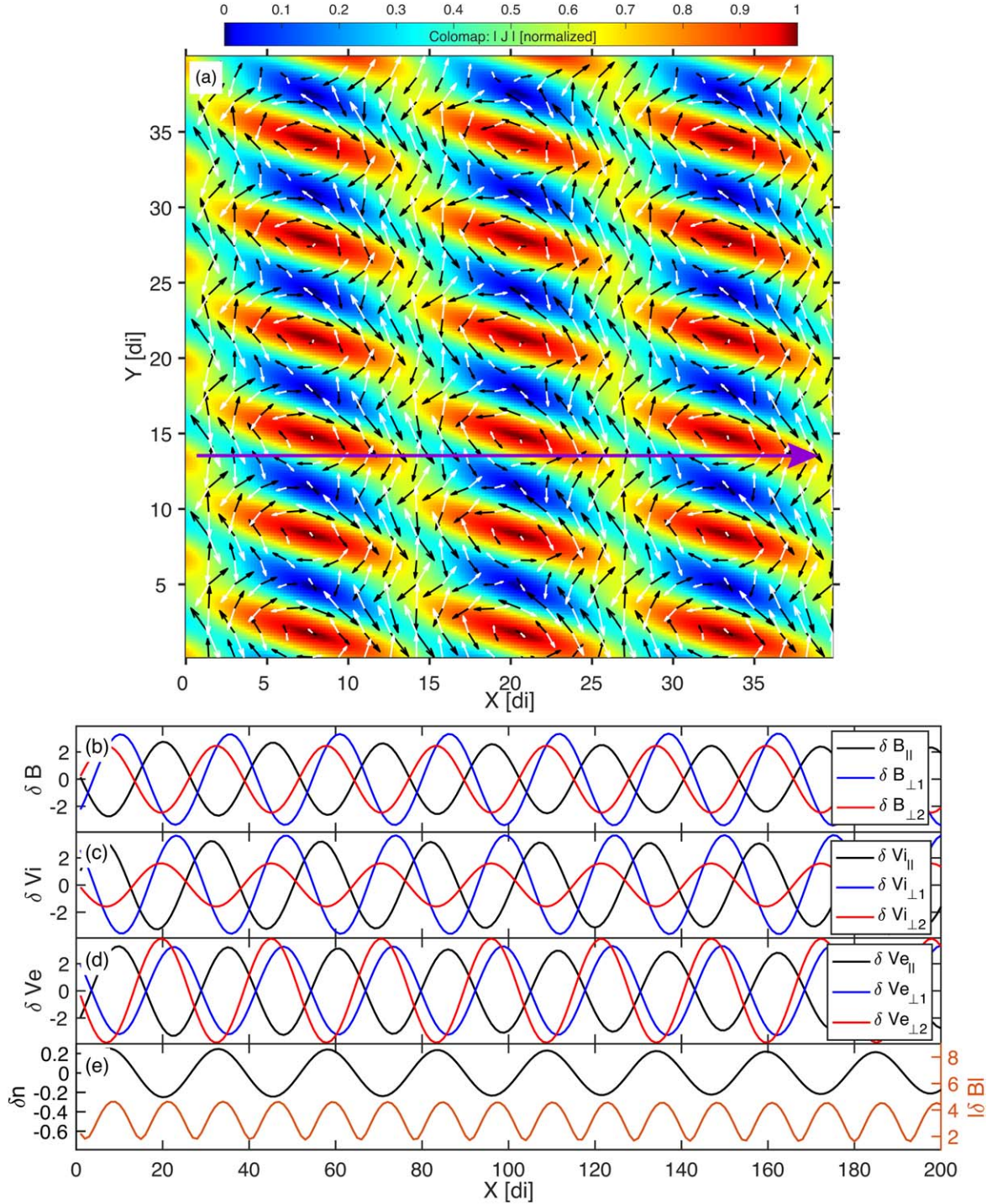


Figure 4. Model result of a vortex array based on the combination of quasi-orthogonal KAWs and KSWs. (a) Model results in the two-dimensional plane perpendicular to the background magnetic field. The color bar represents the magnitude of the current. The black arrows represent the magnetic field direction, and the white arrows represent the ion bulk velocity direction. The long purple arrow represents the trajectory for our one-dimensional sampling. (b)–(e) 1D sampling results of the magnetic field, ion velocity, electron velocity, and number density. The sampling results in the four panels correspond to the observed quantities in Figures 1(f)–(i).

particles ($\delta \mathbf{J} \cdot \delta \mathbf{E}'$) (Figure 3(b)), the ion temperature anisotropy ($\frac{T_{i,\perp}}{T_{i,\parallel}}$) (Figure 3(c)), and the differential energy flux density (Figure 3(d)). We find the following three distinct features for the relation between thermal anisotropy and field-particle energy conversion rate: (1) $\delta \mathbf{E}'_{\perp}$ and $\frac{T_{i,\perp}}{T_{i,\parallel}}$ oscillate in antiphase with the crests (valleys) of $\frac{T_{i,\perp}}{T_{i,\parallel}}$ corresponding to the

valleys (crest) of $\delta \mathbf{E}'_{\perp}$; (2) patches at lower and higher energies in the spectra of differential energy flux recur periodically, mutually misplaced by about 180° in phase, and coincide with the valleys and crests of $\frac{T_{i,\perp}}{T_{i,\parallel}}$, respectively; (3) $\delta \mathbf{J} \cdot \delta \mathbf{E}'$ oscillates at twice the fundamental frequency of the oscillations and stays positive most of the time. Our interpretation of this observation is that the periodic energy conversion (dissipation

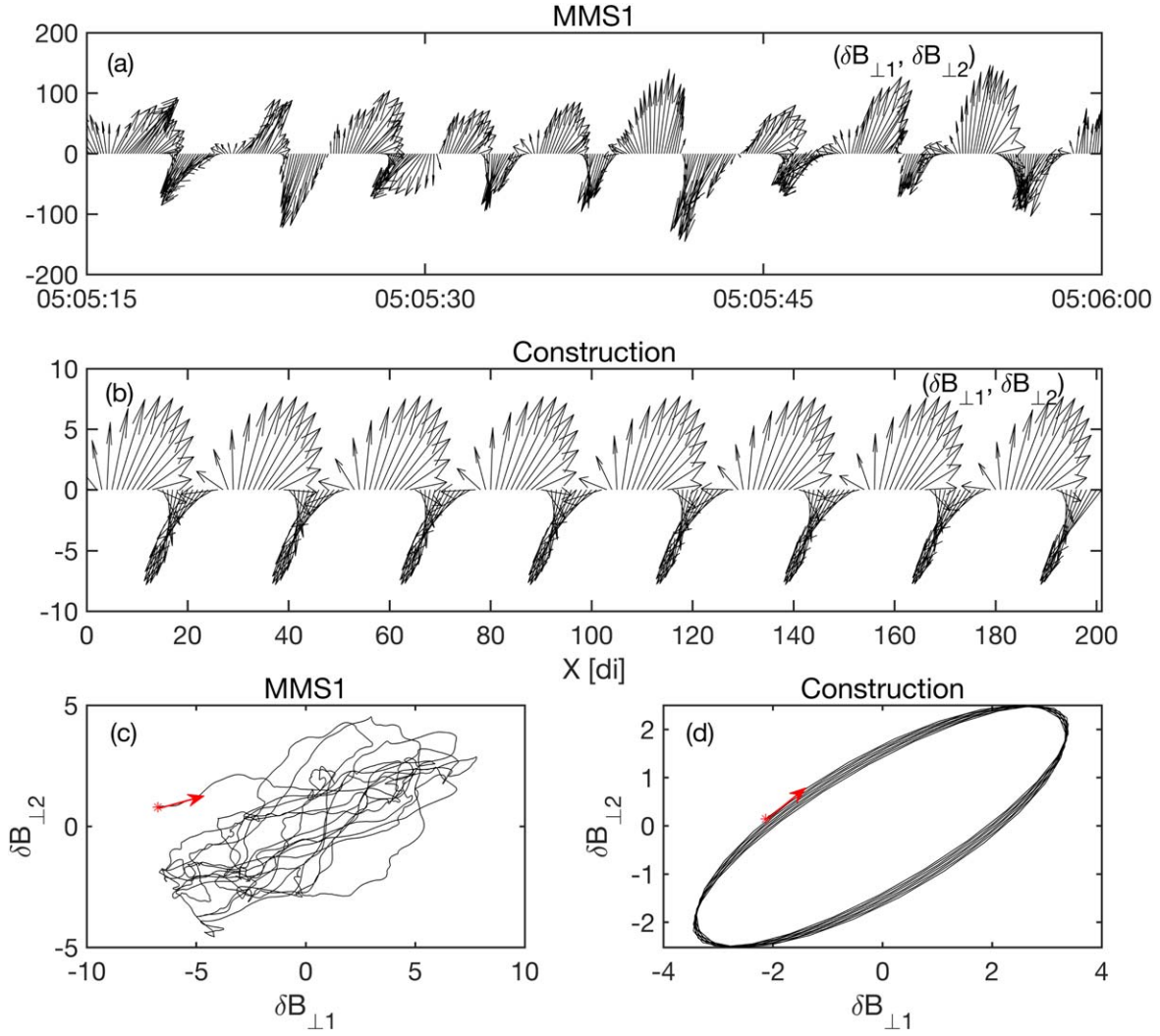


Figure 5. Hodograph representations of the perpendicular magnetic field for MMS1 and in our model. (a) and (b) show the same features. (c) and (d) show a similar polarization. The red arrows indicate the direction of time.

for positive $\delta \mathbf{J} \cdot \delta \mathbf{E}'$) associated with the vortex array is an energy source that modulates the ion temperature anisotropy and the energy spectra (see the animation of Figure 3). The ion population at higher energy potentially leaks from the magnetosphere as ions that are not yet fully thermalized when observed.

3. Vortex Array Model and Comparison with Observations

To explain the correlation between the plasma moments and the energy conversion, we propose a novel model of wave-mode composition taking both KAWs and KSWs into account. In this model, KAWs and KSWs propagate quasi-orthogonally to each other. This behavior leads to a new phenomenon: the formation of vortex arrays. Specifically, we adopt the two-fluid approach of linear plasma wave theory (Zhao 2015; Luo et al. 2022) to calculate the polarization relations in KAWs and KSWs. We combine the KAW and KSW fluctuations and tune the parameters (wavevectors and initial phases) of wave propagation to fit the observational features. We select $kd_i = 1$ for the KAWs and $kd_i = 0.25$ for the KSWs. Our KAWs and KSWs propagate in the quasi-perpendicular direction with $\theta_{kB} = 89^\circ$, where θ_{kB} represents the angle

between the wavevector \mathbf{k} and the background magnetic field \mathbf{B} . In the plane perpendicular to \mathbf{B} , the angle between the KAW and KSW wavevectors is about 104° . The phase difference of our sampled time series is sensitive to this angle, allowing us to explore the consistent angle range, while the phase difference between KAWs and KSWs is 180° . We note that the commonly used wave-mode identification techniques (e.g., SVD-EM method, Santolík et al. 2003; Zhu et al. 2020, or the cross-spectral timing method, Dudok de Wit et al. 1995; Graham et al. 2016) generally only identify one wave mode but are unable to identify two or more wave modes coexisting at a similar observation frequency. Although the k-filtering method can in principle identify multiple wave modes from the distribution of disturbance power in the wavenumber space at a frequency, it is still a challenging task to diagnose and identify different wave modes, which possess different dispersion relations and different polarization properties. In line with the characteristics of quasi-perpendicular propagation for both KAWs and KSWs, we set the propagation angle θ_{kB} of KAWs and KSWs to 89° . We test different parameters (e.g., the wavenumber kd_i of the KAWs and KSWs, azimuthal angle of the wavevector $\phi(k_{KAW,\perp}, k_{KSW,\perp})$, and the phase difference between KAWs and KSWs) to obtain model results that are

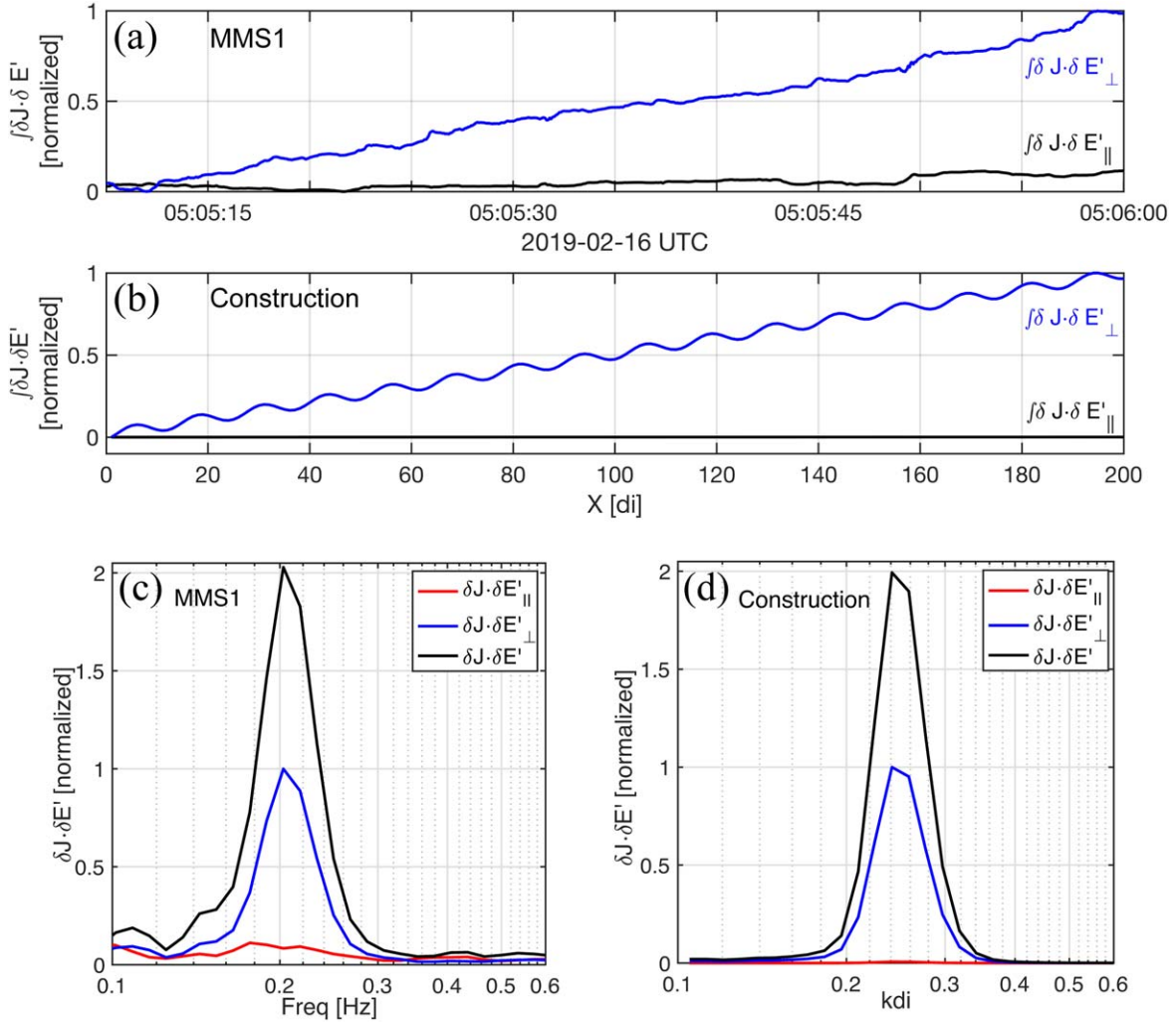


Figure 6. Comparing energy conversion between our MMS1 measurements and our model. (a) Integrated energy conversion parallel and perpendicular to the background magnetic field from our observations. (b) Same as (a), but from our model. (c) Spectrum of energy conversion from our MMS1 measurements. (d) Same as (c), but from our model. The vortex arrays exhibit strong energy conversion in the perpendicular direction and show the same features as the observed energy conversion.

consistent with the observations and select the corresponding parameters.

We illustrate the dynamic evolution of the vortex array - composed of the two quasi-orthogonal waves within a 3D space of size $200d_i \times 200d_i \times 200d_i$. A subset of the vortex array with a sub-area of $40d_i \times 40d_i$ on the plane perpendicular to the background magnetic field direction is presented in Figure 4(a). The magnetic field vectors (black arrows) and the ion velocity vectors (white arrows) show magnetic field vortices and velocity vortices that occur periodically. The current density at the X-points is different from that at the O-points: the current intensity at the O-points has a local maximum, while the current density at the X-points has a local minimum. This difference comes from the fact that the shear of the magnetic fields around the X-points cancels, while the shear of the magnetic fields around the O-points is additive. Although the magnetic field configuration between the two vortices in the vortex array has an X-type geometry similar to that of magnetic reconnection, no reconnection features (i.e., jets) are found in our observations. This indicates that vortex arrays may be a type of non-reconnecting current sheets.

We sample our model results along a one-dimensional trajectory shown as the purple arrow in Figure 4(a). The result shows a remarkable agreement with our MMS observations. The phase relationship among the three components of the magnetic field (Figure 4(b)) is consistent with that in the MMS observations (Figure 1(a)), and so are the ion velocity components between the model (Figure 4(c)) and the observations (Figure 1(b)). Due to the contribution from KSWs, the magnetic field and ion velocity (Figure 4(b), (c)) in our model are not exactly anticorrelated, matching with the MMS observations (Figure 1(a), (b)). The polarization hodograph of the perpendicular magnetic field components also shows the same characteristics between the observations and our model results (Figure 5). The observed electron bulk velocity fluctuations have contributions from smaller-scale disturbances, which are not included in our model. Consistent with our observations (Figure 1(d)), the model result shows large fluctuations in the number density (Figure 4(e)). The modeled fluctuations in the magnitude of the magnetic field (Figure 4(e)) have twice the frequency (Figure 4(e)). These comparisons suggest that the MMS event is likely to be composed of vortex arrays of KAWs and KSWs.

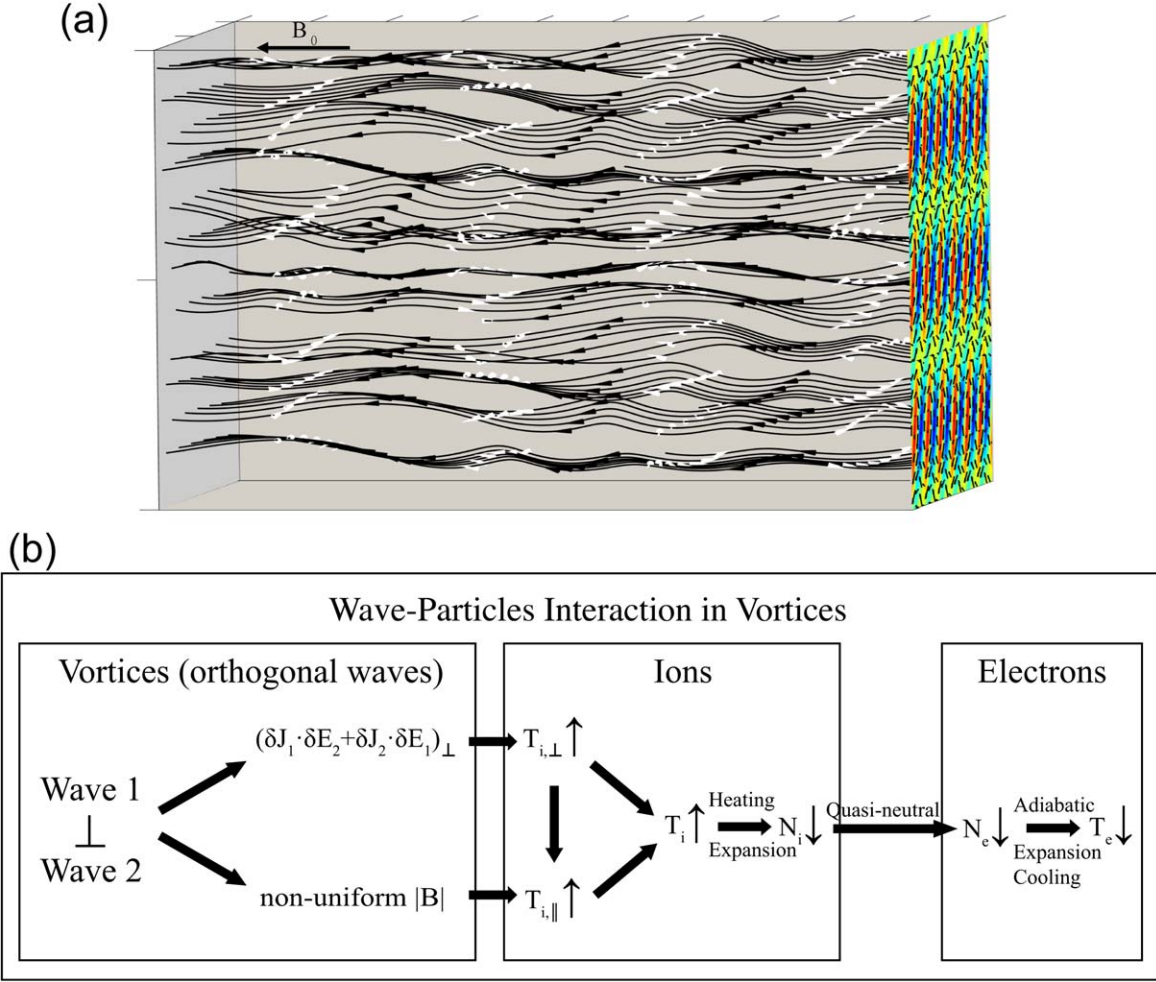


Figure 7. 3D vortex arrays and wave-particle interactions in vortex arrays. (a) 3D construction of vortex arrays consisting of waves with quasi-orthogonal wavevectors. The black lines represent magnetic field lines. We show the direction of the magnetic field (black arrows) and ion velocity (white arrows) along the field lines. The surface on the right-hand side of the box is the same as that in Figure 3(a). (b) The process of ion and electron thermalization through orthogonal waves. The vortex arrays build a connection between waves and structures and successfully explain the observed data. The corresponding animation of panel (a) is available in the online version of this paper. This animation shows the 3D construction of vortex arrays from multiple perspectives and at different time instances. The animation runs from the top view to the side view and then runs for a period of the vortex evolution.

For plane-wave KAWs, due to their phase lag of about 90° between $\delta \mathbf{J}_\perp$ and $\delta \mathbf{E}'_\perp$, the period-average $\langle \delta \mathbf{J}_\perp \cdot \delta \mathbf{E}'_\perp \rangle$ is near zero. Hence, purely plane KAWs cannot explain the strong global/net energy conversion in this event. However, in the vortex array, we find that the combination of the two wave modes enhances the perpendicular energy conversion with $\langle \delta \mathbf{J}_{\perp, \text{KAW}} \cdot \delta \mathbf{E}'_{\perp, \text{KSW}} + \delta \mathbf{J}_{\perp, \text{KSW}} \cdot \delta \mathbf{E}'_{\perp, \text{KAW}} \rangle$ being significantly greater than zero. After employing the code PKUES (Plasma Kinetic Unified Eigenmode Solutions) to obtain the polarization relations of KAWs and KSWs, we calculate the $\delta \mathbf{J} \cdot \delta \mathbf{E}'$, which describes an energy conversion from fields to particles when it is positive, caused by the vortex array along the sampling path (the purple line in Figure 4). The plasma parameters used in PKUES are $n_p = n_e = 14.7 \text{ cm}^{-3}$, $\frac{T_{p,\perp}}{T_{p,\parallel}}$, $\frac{T_{e,\perp}}{T_{e,\parallel}} = 1.02$, where n_p is the proton number density, n_e is the electron number density, $\frac{T_{p,\perp}}{T_{p,\parallel}}$ is the proton thermal anisotropy, and $\frac{T_{e,\perp}}{T_{e,\parallel}}$ is the electron thermal anisotropy. In our model (Figure 6(b)), the integrated $\delta \mathbf{J}_\perp \cdot \delta \mathbf{E}'_\perp$ shows a clear net increase, consistent with the observed profile (Figure 6(a)).

The integrated $\delta \mathbf{J}_\perp \cdot \delta \mathbf{E}'_\perp$ for a pure KSW is not zero, and thus greater than for a pure KAW. For a vortex array composed of KAWs and KSWs, the integrated $\delta \mathbf{J}_\perp \cdot \delta \mathbf{E}'_\perp$ is even greater. The modeled spectrum of $\delta \mathbf{J}_\perp \cdot \delta \mathbf{E}'_\perp$ (Figure 6(d)) also has the same energy conversion features as observed (Figure 6(c)). We calculate the energy conversion rate under different angles and phases between KAWs and KSWs. We find the most consistent angle falls in the range of $[70^\circ, 110^\circ]$, which means that KAWs and KSWs propagate quasi-orthogonally. According to our test, the phase difference between KAWs and KSWs does not significantly affect the energy conversion rate. For $\theta_{k\mathbf{B}}$ between $85^\circ \sim 95^\circ$, the same wave mode has similar electric polarization, magnetic polarization, Alfvén ratio, and compressibility. Hence, in the case of two wave modes with quasi-perpendicular wavevectors, the energy conversion rate does not depend sensitively on $\theta_{k\mathbf{B}}$. The agreement between our model and our observations successfully demonstrates that vortex arrays composed of quasi-orthogonal KAW and KSW modes provide a new and promising mechanism for the conversion of the turbulence energy and the modulation of the ion temperature and energy flux in the magnetosheath.

4. Summary and Discussion

The quasi-orthogonal propagation of KAWs and KSWs results in a spatially inhomogeneous distribution of the magnetic field. Its perpendicular components form a vortex array in the plane perpendicular to the background magnetic field direction (Figure 7(a) and the corresponding animation). We illustrate the energization processes for the ions and electrons in Figure 7(b). The ions undergo nonadiabatic processes, while the electrons obey adiabatic routes. The ions are transversely energized in the perpendicular direction by the energy conversion of the vortex array via positive $\delta \mathbf{J}_\perp \cdot \delta \mathbf{E}'_\perp$. The Lorentz forces with the transverse magnetic field components of the vortex array divert the ion motion and convert the kinetic energy from the perpendicular to the parallel degrees of freedom. Finally, the total ion temperature increases. The density of the heated ions then decreases due to local expansion effects. Along with the expansion, the electrons are cooled adiabatically in the absence of kinetic waves at electron scales. The electrons with small gyro-radii are trapped in the longitudinal magnetic mirror structures, leading to the modulation of the pitch angle distribution.

Our analysis reveals the existence of a vortex array in the magnetosheath by comparing MMS observations with model results. The vortex array is composed of KAWs and KSWs, which propagate quasi-orthogonally to each other. Such a vortex array enables a strong transverse energy conversion and hence may be responsible for the efficient nonadiabatic heating of ions. The longitudinal magnetic mirror structure and density compression lead to the quasi-adiabatic heating of the electrons. There are multiple mechanisms for the generation of KAWs and KSWs. KAWs can be generated from the anisotropic cascade of MHD-scale Alfvénic turbulence (Howes et al. 2008; He et al. 2012; Zhao et al. 2013), and MHD-scale Alfvén waves may decay nonlocally into KAWs and KSWs (Zhao et al. 2014a). Mirror modes may also evolve into KAWs in their nonlinear phase (Wu et al. 2001). Since the excitation threshold for the mirror-mode instability is more easily met downstream of the quasi-perpendicular bow shock than downstream of the quasi-parallel bow shock, we speculate that there will be more KAWs downstream of the quasi-perpendicular bow shock. In hybrid simulations, KSWs appear downstream of the quasi-parallel bow shock (Hao et al. 2018). Therefore, we reason that both KAWs and KSWs can exist in the downstream transition region between quasi-parallel and quasi-perpendicular shock geometries. The mixing of KAWs and KSWs in the transition region can naturally lead to the formation of vortex arrays. We find some other similar events to the one analyzed in this work, which have similar frequencies of the fluctuating quantities. Since Alfvén waves and slow-mode-like pressure-balanced structures are often observed to coexist in the turbulent solar wind (Howes et al. 2012; He et al. 2015a; Yang et al. 2017), it is an option worth considering that vortex arrays could also exist in the interplanetary solar wind with Alfvénic and compressive turbulence. The vortex array is potentially an important feature in these turbulent environments and contributes to the energy conversion therein. Thus, the vortex array is of great significance for the understanding of the energy conversion processes between fields and particles in plasmas and their efficiency in universal collisionless plasma turbulence.

The vortex array is accompanied by an increased energy conversion when the propagation angle of the two waves is

between 70° and 110° . Indeed, the quasi-orthogonal propagation of the two waves presents a limit for the existence of vortex arrays, but a not very strict one. In a magnetized turbulent plasma environment, such as the solar wind, the anisotropic cascade of Alfvénic turbulence prefers to cascade energy toward increasingly more perpendicular wavevectors, which tends to produce quasi-perpendicular kinetic wave modes, and the perpendicular wavevectors can be quasi-orthogonal (Wang et al. 2020; Zhang et al. 2022). Quasi-perpendicular and quasi-orthogonal Alfvén waves and slow magnetoacoustic waves in solar wind turbulence and their kinetic scale counterparts have an essential influence on the energization of the solar wind (He et al. 2015b). Therefore, we conjecture that the physics of vortex arrays deserves a more detailed analysis in the future, which may help better understand the nature of wave-like turbulence and its dissipative heating effects.

We are grateful to the teams of the MMS mission for providing the calibrated measurement data. We also thank the team of 3DView maintained mainly by IRAP/CNES. The work at Peking University is supported by National Key R&D Program of China (2021YFA0718600 and 2022YFF0503800), by NSFC (42241118, 42174194, 42150105, and 42204166), and by CNSA (D050106). C.H. from Peking University is also supported by the China Scholarship Council. D.D. from Peking University is also supported by China Postdoctoral Science Foundation (2022M720213). W.L. from NSSC is supported by NSFC grant 41974170. D.V. from UCL is supported by the STFC Ernest Rutherford Fellowship ST/P003826/1 and STFC Consolidated Grants ST/S000240/1 and ST/W001004/1. T. W. from YNU is supported by the NSFC grant 42104157 and the start-up funding from YNU. We appreciate valuable comments from Q.G. Zong and X.Z. Zhou at Peking University, and Y. Wang at Harbin Institute of Technology in Shenzhen. We use the 3Dview Java application tool to visualize the MMS location (Figure 1(a)), the magnetopause geometry, the bow shock geometry, and the magnetic field lines in the magnetosphere. We use the Autoplot application developed under the NASA Virtual Observatories for Helio-physics program to prepare Figure 2. The PKUES code is available at <https://github.com/PKU-Heliosphere/PKUES>.

ORCID iDs

Chuanpeng Hou  <https://orcid.org/0000-0001-7205-2449>
 Jiansen He  <https://orcid.org/0000-0001-8179-417X>
 Die Duan  <https://orcid.org/0000-0002-6300-6800>
 Xingyu Zhu  <https://orcid.org/0000-0002-1541-6397>
 Daniel Verscharen  <https://orcid.org/0000-0002-0497-1096>
 Terry Liu  <https://orcid.org/0000-0003-1778-4289>
 Teyan Wang  <https://orcid.org/0000-0003-3072-6139>

References

- Alexandrova, O., Mangeney, A., Maksimovic, M., et al. 2006, *JGRA*, **111**, A12208
 Artemyev, A., Rankin, R., & Blanco, M. 2015, *JGRA*, **120**, 10305
 Burch, J., Moore, T., Torbert, R., & Giles, B. 2016a, *SSRv*, **199**, 5
 Burch, J., Torbert, R., Phan, T., et al. 2016b, *Sci*, **352**, aaf2939
 Chasapis, A., Matthaeus, W. H., Parashar, T. N., et al. 2018, *ApJL*, **856**, L19
 Chen, C., Klein, K., & Howes, G. G. 2019, *NatCo*, **10**, 1
 Chen, C. H. K., & Boldyrev, S. 2017, *ApJ*, **842**, 122
 Dai, L., Wang, C., Cai, Z., et al. 2020, *FrP*, **8**, 89

- Drake, J. F., Swisdak, M., Cattell, C., et al. 2003, *Sci*, 299, 873
- Dudok de Wit, T., Krasnosel'skikh, V. V., Bale, S. D., et al. 1995, *GeoRL*, 22, 2653
- Escoubet, C., Fehring, M., & Goldstein, M. 2001, *AnGeo*, 19, 1197
- Fu, H. S., Cao, J. B., Vaivads, A., et al. 2016, *JGRA*, 121, 1263
- Gary, S. P., Fuselier, S. A., & Anderson, B. J. 1993, *JGRA*, 98, 1481
- Gershman, D. J., F-Vinas, A., Dorelli, J. C., et al. 2017, *NatCo*, 8, 14719
- Graham, D. B., Khotyaintsev, Y., Vaivads, A., & Andre, M. 2016, *JGRA*, 121, 3069
- Hao, Y., Lu, Q., Gao, X., et al. 2018, *ApJ*, 861, 57
- Hasegawa, H., Zhang, H., Lin, Y., et al. 2012, *JGRA*, 117, A09214
- He, J., Duan, D., Wang, T., et al. 2019, *ApJ*, 880, 121
- He, J., Marsch, E., Tu, C., Yao, S., & Tian, H. 2011, *ApJ*, 731, 85
- He, J., Pei, Z., Wang, L., et al. 2015a, *ApJ*, 805, 176
- He, J., Tu, C., Marsch, E., et al. 2015b, *ApJL*, 813, L30
- He, J., Tu, C., Marsch, E., & Yao, S. 2012, *ApJ*, 749, 86
- He, J., Zhu, X., Verscharen, D., et al. 2020, *ApJ*, 898, 43
- Hoilijoki, S., Palmroth, M., Walsh, B. M., et al. 2016, *JGRA*, 121, 4191
- Hou, C., He, J., Zhu, X., & Wang, Y. 2021, *ApJ*, 908, 237
- Howes, G. G., Bale, S. D., Klein, K. G., et al. 2012, *ApJL*, 753, L19
- Howes, G. G., Cowley, S. C., Dorland, W., et al. 2008, *JGRA*, 113, A05103
- Huang, S. Y., Sahraoui, F., Yuan, Z. G., et al. 2018, *ApJ*, 861, 29
- Lion, S., Alexandrova, O., & Zaslavsky, A. 2016, *ApJ*, 824, 47
- Lucek, E. A., Dunlop, M. W., Balogh, A., et al. 1999, *GeoRL*, 26, 2159
- Luo, Q., He, J., Cui, J., et al. 2020, *ApJL*, 904, L16
- Luo, Q., Zhu, X., He, J., et al. 2022, *ApJ*, 928, 36
- Masood, W., Schwartz, S., Maksimovic, M., & Fazakerley, A. 2006, *AnGeo*, 24, 1725
- Narita, Y., & Marsch, E. 2015, *ApJ*, 805, 24
- Osman, K. T., Matthaeus, W. H., Gosling, J. T., et al. 2014, *PhRvL*, 112, 215002
- Roberts, O. W., Li, X., Alexandrova, O., & Li, B. 2016, *JGRA*, 121, 3870
- Roberts, O. W., Toledo-Redondo, S., Perrone, D., et al. 2018, *GeoRL*, 45, 7974
- Santolík, O., Parrot, M., & Lefeuvre, F. 2003, *RaSc*, 38, 1010
- Schwartz, S., Burgess, D., & Moses, J. 1996, *AnGeo*, 14, 1134
- Soucek, J., Lucek, E., & Dandouras, I. 2008, *JGRA*, 113, A04203
- Sundkvist, D., Krasnosel'skikh, V., Shukla, P. K., et al. 2005, *Natur*, 436, 825
- Sundkvist, D., Retinò, A., Vaivads, A., & Bale, S. D. 2007, *PhRvL*, 99, 025004
- Tu, C.-Y., & Marsch, E. 1995, *SSRv*, 73, 1
- Wan, M., Matthaeus, W. H., Roytershteyn, V., et al. 2015, *PhRvL*, 114, 175002
- Wang, R., Lu, Q., Nakamura, R., et al. 2016, *NatPh*, 12, 263
- Wang, T., Alexandrova, O., Perrone, D., et al. 2019, *ApJL*, 871, L22
- Wang, T., He, J., Alexandrova, O., Dunlop, M., & Perrone, D. 2020, *ApJ*, 898, 91
- Wang, X., Tu, C., He, J., Marsch, E., & Wang, L. 2013, *ApJL*, 772, L14
- Wu, B. H., Wang, J. M., & Lee, L. C. 2001, *GeoRL*, 28, 3051
- Wu, D. J., Feng, H. Q., Li, B., & He, J. S. 2016, *JGRA*, 121, 7349
- Wu, H., Tu, C., Wang, X., He, J., & Yang, L. 2020, *ApJL*, 904, L8
- Yang, L., He, J., Tu, C., et al. 2017, *ApJ*, 836, 69
- Yao, S. T., Shi, Q. Q., Guo, R. L., et al. 2020, *ApJ*, 897, 137
- Yao, S. T., Shi, Q. Q., Liu, J., et al. 2018, *JGRA*, 123, 5561
- Zhang, J., Huang, S. Y., He, J. S., et al. 2022, *ApJL*, 924, L21
- Zhao, J. 2015, *PhPI*, 22, 042115
- Zhao, J., Voitenko, Y., Wu, D., & De Keyser, J. 2014a, *ApJ*, 785, 139
- Zhao, J., Voitenko, Y., Yu, M., Lu, J., & Wu, D. 2014b, *ApJ*, 793, 107
- Zhao, J. S., Wang, T. Y., Dunlop, M. W., et al. 2019, *GeoRL*, 46, 4545
- Zhao, J. S., Wu, D. J., & Lu, J. Y. 2013, *ApJ*, 767, 109
- Zhu, X., He, J., Verscharen, D., Duan, D., & Bale, S. D. 2020, *ApJL*, 901, L3